# Vector Resonance Multimode Instability

S.V Sergeyev[1*], H. Kbashi[1], N. Tarasov[1], Yu. Loiko[1], and S. A. Kolpakov[1]

[1]*Aston Institute of Photonic Technologies, Aston University, Birmingham, B4 7ET, United Kingdom*

**Corresponding author e-mail address: s.sergeyev@aston.ac.uk*

**The modulation and multimode instabilities are the main mechanisms which drive spontaneous spatial and temporal patterns formation in a vast number of nonlinear systems ranging from biology to the laser physics. Using Er-doped fiber laser as a test bed, here for the first time we demonstrate both experimentally and theoretically a new type of a low threshold vector resonance multimode instability which inherits features of multimode and modulation instabilities. The same as for the multimode instability, the large number of longitudinal modes can be excited without modes synchronization. To enable modulation instability, we modulate the state of polarization of the lasing signal with the period of the beat length by adjustment of the in-cavity birefringence and the state of polarization of the pump wave. As a result, we show regimes tunability from complex oscillatory to periodic with longitudinal modes synchronization in the case of the resonance matching between beat and cavity lengths. Apart from the interest in laser physics for unlocking tunability and stability of dynamic regimes, the proposed mechanism of the vector resonance multimode instability can be of fundamental interest for nonlinear dynamics of various distributed systems.**

Keywords: multimode instability, fiber laser, self-mode locking, polarization

Modulation instability (MI) is a term widely used to characterize mechanism which drives the emergence of spatial and temporal patterns in different systems including fluids, granular media, plasma, nonlinear optics and lasers [1-9]. For example, the Benjamin-Feir instability (BFI) characterizes the origin of the structures with the wave numbers $k$ and $-k$ due to synchronization with homogeneous mode of $k=0$ trough nonlinearity [1, 4]. In the case of the Faraday instability, spatial structures will arise as a result of an external uniform modulation [1, 5, 9]. Recently discovered a new type of MI, namely dissipative parametric instability

(DPI) [9], is based on periodic antiphase modulation of spectrally dependent losses and leads to the formation of stable patterns in one- and two-dimensional systems. Unlike different types of MIs, in the case of multimode Risken-Nummedal-Graham-Haken (RNGH) instability the typical scenario in the laser with unidirectional cavity and homogeneously broadened active medium is the presence of the second laser threshold exceeding the first in nine times in terms of the pump power [10-12]. Exceeding the second threshold results in excitation of a large number of the longitudinal spatial modes and generation of the pulse train with period of the cavity round-trip time. The history of the multimode Risken-Nummedal-Graham-Haken (RNGH) instability started in 1968. Since then, the extensive theoretical and experimental study of Er-doped fiber lasers revealed decreased second lasing threshold to the values slightly exceeding the value for the first threshold [13-18]. However, there is still an issue related to the accounting for the vector nature of the fiber laser dynamics which it typically present in the experiments on RNGH instability [14, 17]. This vector nature comprises tuning in-cavity birefringence and the state of polarization (SOP) of the pump wave with the help of polarization controllers and observation of the corresponding tunability of the self-pulsing in the form of stable and unstable pulse trains [14, 17, 19].

In this Letter, for the first time we address the challenge related to accounting for vector nature of the laser dynamics by demonstrating theoretically and experimentally a new type of vector resonance multimode instability which inherits some features of MI and multimode instability in terms of tunability of the laser dynamics from the turbulent to the stable pulse train similar to the laser mode-locking regime. We have justified experimentally and theoretically that increased in-cavity birefringence strength causes spatial modulation of the SOP of the in-cavity lasing field (with a period related to the beat length) and so leads through dispersion relation to the emergence of the additional satellite frequencies with the frequency splitting proportional to the birefringence strength. When the splitting is approaching the fundamental frequency inversely proportional to the photon round trip time, parametric resonance results in longitudinal modes synchronization and emergence of the pulse train with the narrow pulse width in the same way as the injection locking [20]. In the experiments, we use special laser configuration and pump power of about hundred times less to exclude mode locking based on nonlinear polarization rotation [21, 22].

The schematic of the unidirectional cavity fiber laser is shown in Fig. 1 (a) (details are found in Supplementary Material [23]).

The first lasing threshold for the continuous wave (CW) regime was found in terms of the pump power as 16 mW whereas the second threshold of the multimode instability was of 18 mW. The orientations of the paddles of the polarization controllers (POC1 and POC2) were measured with respect to the vertical position. The paddle of POC1 was set at $\theta_1$=-59$^0$ whereas paddle of POC2 was set at four different positions, namely $\theta_2$=-80$^0$,-78$^0$,-74$^0$,-69$^0$. To characterize the polarization laser dynamics at the slow scale, we use polarimeter (resolution of 1 $\mu$s and combined 16 frames with 1024 samples in each frame) to measure the normalized Stokes parameters $s_1$, $s_2$, $s_3$ and degree of polarization (DOP) which are related to the output powers of two linearly cross-polarized SOPs $|u|^2$ and $|v|^2$, and phase difference between them $\Delta\varphi$ as follows:

$$S_0 = |u|^2 + |v|^2,\ S_1 = |u|^2 - |v|^2,\ S_2 = 2|u||v|\cos\Delta\varphi,\ S_3 = 2|u||v|\sin\Delta\varphi,$$
$$s_i = \frac{S_i}{\sqrt{S_1^2 + S_2^2 + S_3^2}},\quad DOP = \frac{\sqrt{S_1^2 + S_2^2 + S_3^2}}{S_0},(i = 1,2,3) \tag{1}$$

The results on polarization dynamics are shown in Fig.1 (b, c). As follows from the Fig.1(b), the size of the sport on the Poincaré sphere indicates the deviation of N-fold beat length from the cavity length, i.e. by decreasing the size of the spot by adjusting $\theta_2$ demonstrates that N-fold beat length is approaching the cavity length. As follows from Fig. 1 (c), small oscillations in the output power $S_0$ and the phase difference $\Delta\varphi$ along with DOP of 40% indicates that the laser dynamics is fast with the time scale smaller than 1 $\mu$s for POC2 setting at $\theta_2$=-80$^0$. The further tuning the POC2 demonstrates the suppression of the fast dynamics. The constant outputs and high (over 80%) DOP in Fig. 1 (c) indicate the stable mode locking accompanied with the stable SOP locking (matching N-fold beat length to the cavity length).

Though the fundamental frequency was of 325.2 kHz, the radiofrequency (RF) spectrum evolution driven by adjustment of the in-cavity polarization controller was resolved better in the case of 1000$^{th}$ harmonic, i.e. around frequency of about 325.2 MHz (Fig.2 (a1-d1)). The RF spectrum shown in Fig 2(a1-d1) reveals three types of peaks. The central peak corresponds to the 1000$^{th}$ harmonic of the fundamental self-mode locking frequency, the two satellites adjustable with the help of the POC2 and two closely located to the fundamental frequency satellites position of which is independent on POC2 adjustment. The origin of these satellites is discussed further based on the theoretical results. As follows from the Fig.1(b, c) and Fig.2(a1-d1) , the adjustment of the beat

length to the cavity length was done inside very narrow margins where only birefringence-dependent satellites from the neighboring to 325.2 MHz lines are visible. As follows from corresponding Fig.2 (a2-d2), this adjustment results in regime stabilization similar to mode-locking for the case when satellites match the main line (Fig. 2 (d2)). Unlike RHGM instability demonstrating oscillations close the harmonic with the photon round trip time period, the pulse train in Fig.2 (d2) has the pulse width of 40 ns which is much less than the round trip time of 3 $\mu$s. This indicates the excitation of many longitudinal modes along with their relative phase synchronization.

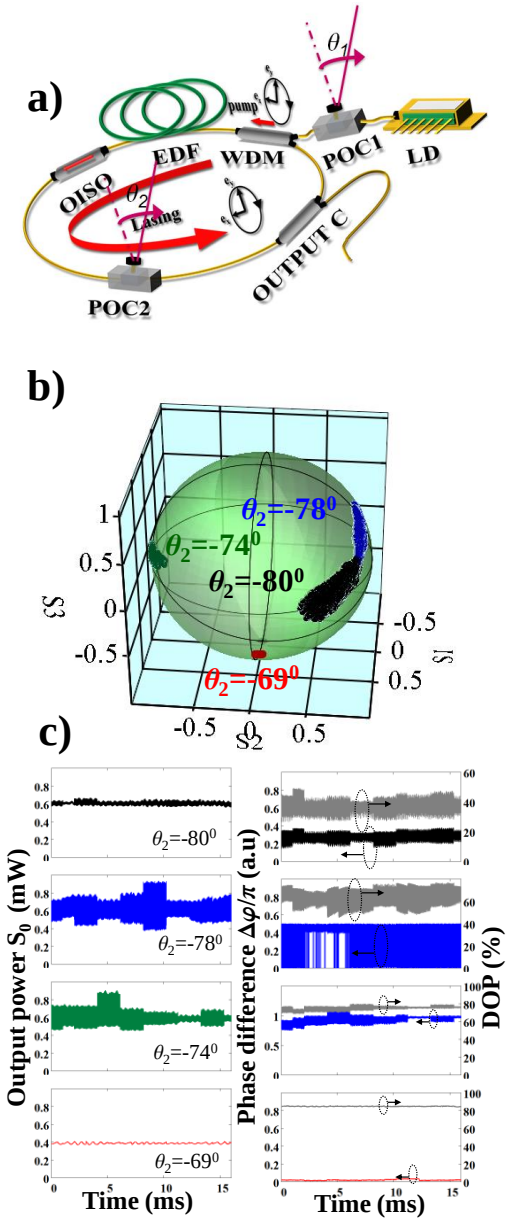

FIG. 1 (color online) (a) Erbium doped fiber laser. EDF: erbium-doped fiber; LD: l480 nm laser diode for pump; POC1 and POC2: polarization controllers, OISO: optical isolator; WDM: wavelength division multiplexer (WDM), OUTPUT C: 80:20 output coupler. (b) The map of the states of polarization on the Poincaré sphere (b) output power ($S_0$) (c left) and corresponding phase difference between linearly polarized modes and DOP (c right) for different setting of the POC2: $\theta_2$=-80$^0$, -78$^0$; -74$^0$; -69$^0$. IN1: the state of polarization with the ellipticity $\delta$ is equivalent to the linearly polarized pump oriented at an angle $\psi$ (tan($\psi$)=$\delta$ ) to the axis $\mathbf{e}_x$.

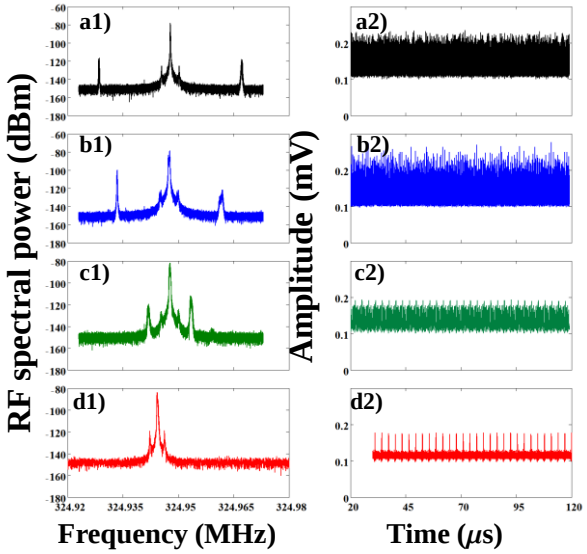


FIG.2 (color online) The RF spectrum (a1-d1) and corresponding oscillograms (a2-d2) for different setting of the POC2: a1, a2) $\theta_2$=-80$^0$; b1, b2) $\theta_2$=-78$^0$; c1, c2) $\theta_2$=-74$^0$; d1, d2) $\theta_2$=-69$^0$.

The experimental results can be well understood based on the vector model of an Er-doped fiber laser. The following rate equations are derived from the model suggested by Sergeyev et al. [24, 25]:

$$\frac{\partial S_0}{\partial z}+\frac{\partial S_0}{\partial t}=\left(\frac{2\alpha_1 f_1}{1+\Delta^2}-2\alpha_2\right)S_0+\frac{2\alpha_1 f_2}{1+\Delta^2}S_1+\frac{2\alpha_1 f_3}{1+\Delta^2}S_2,$$

$$\frac{\partial S_1}{\partial z}+\frac{\partial S_1}{\partial t}=\gamma S_2 S_3+\left(\frac{2\alpha_1 f_1}{1+\Delta^2}-2\alpha_2\right)S_1+\frac{2\alpha_1 f_2}{1+\Delta^2}S_0$$

$$-\frac{2\alpha_1 f_3\Delta}{1+\Delta^2}S_3,$$

$$\frac{\partial S_2}{\partial z}+\frac{\partial S_2}{\partial t}=-\gamma S_1 S_3+\frac{2\alpha_1 f_3}{1+\Delta^2}S_0+\left(\frac{2\alpha_1 f_1}{1+\Delta^2}-2\alpha_2\right)S_2+$$

$$\left(\frac{2\alpha_1 f_2\Delta}{1+\Delta^2}-2\beta\right)S_3,$$

$$\frac{\partial S_3}{\partial z}+\frac{\partial S_3}{\partial t}=\frac{2\alpha_1\Delta f_3}{1+\Delta^2}S_1-\frac{2\alpha_1\Delta f_2}{1+\Delta^2}S_2+2\beta S_2+$$

$$\left(\frac{2\alpha_1 f_1}{1+\Delta^2}-2\alpha_2\right)S_3,$$

$$\frac{df_1}{dt}=\varepsilon\left[\frac{(\chi_s-1)I_p}{2}-1-\left(1+\frac{I_p\chi_p}{2}+d_1S_0\right)f_1-\left(d_1S_1+\frac{I_p}{2}\xi\right)f_2-d_1S_2f_3\right],$$

$$\frac{df_2}{dt}=\varepsilon\left[\xi\frac{I_p(\chi_s-1)}{4}-\left(\frac{I_p\chi_p}{2}+1+d_1S_0\right)f_2-\left(\frac{I_p\chi_p}{2}\xi+d_1S_1\right)\frac{f_1}{2}\right],$$

$$\frac{df_3}{dt}=-\varepsilon\left[\frac{d_1S_2f_1}{2}+\left(\frac{I_p\chi_p}{2}+1+d_1S_0\right)f_3\right].$$

(2)

Here time is normalized to the round trip and length - to the cavity length; $S_i$ $(i=0,1,2,3)$ are the Stokes parameters ($S_0$ is the output power, pump and lasing powers are normalized to the corresponding saturation powers: $S_0^2=S_1^2+S_2^2+S_3^2$); $\alpha_1$ is the total absorption of erbium ions at the lasing wavelength, $\alpha_2$ is the total insertion losses in cavity, $\beta$ is the birefringence strength ($2\beta=2\pi L/L_b$ , $L_b$ is the beat length); $\xi=(1-\delta^2)/(1+\delta^2)$ is parameter of the pump anisotropy, $\delta$ is the ellipticity of the pump wave, $\varepsilon=\tau_R/\tau_{Er}$ is the ratio of the round trip time $\tau_R$ to the lifetime of erbium ions at the first excited level $\tau_{Er}$; $\chi_{p,s}=(\sigma_a^{(s,p)}+\sigma_e^{(s,p)})/\sigma_a^{(s,p)}$, ($\sigma_a^{(s,p)}$ and $\sigma_e^{(s,p)}$ are absorption and emission cross sections at the lasing (s) and pump (p) wavelengths); $\Delta$ is the detuning of the lasing wavelength with respect to the maximum of the gain spectrum (normalized to the gain spectral width; $d_1=\chi/\pi(1+\Delta^2)$; functions $f_i$ $(i=1,2,3)$ are related to the angular distribution of the excited ions $n(\theta)$ expanded into a Fourier series as follows [24-26]:

$$n(\theta)=\frac{n_0}{2}+\sum_{k=1}^{\infty}n_{1k}\cos(k\theta)+\sum_{k=1}^{\infty}n_{2k}\sin(k\theta),$$
$$f_1=\left(\chi\frac{n_0}{2}-1\right)+\chi\frac{n_{12}}{2},$$
$$f_2=\left(\chi\frac{n_0}{2}-1\right)-\chi\frac{n_{12}}{2}, f_3=\chi\frac{n_{22}}{2}. \quad (3)$$

Equations (2) have been derived under the approximation that the dipole moments of the absorption and emission transitions for erbium doped silica are located in the plane orthogonal to the direction of the light propagation [24-26]. Unlike more general assumption of the 3D orientation distribution of the dipole orientations [27, 28], approximation in the form of Eqs. (3) allows getting the finite dimension system presented by Eqs. (2) where only $n_0$, $n_{12}$, and $n_{21}$ components contribute to the vector dynamics. As follows from the Eqs. (2) and Fig. 1 (IN1) the state of polarization with the ellipticity $\delta$ is equivalent to the linearly polarized pump oriented at an angle $\psi$ ($\tan(\psi)=\delta$ ). As follows from the structure of Eqs. (2), birefringence in the laser cavity comprises two parts, viz. birefringence of the passive fiber combined with birefringence induced by the in-cavity polarization controller ( $2\beta=2\pi L/L_b$ ) and birefringence caused by polarization hole burning in the active fiber ( $\Delta_\beta=2\alpha_1 f_2\Delta/(1+\Delta^2)$ ) . In the experiments, we set the pump power at 18 mW which is much less than values (approx. 800 mW) required for mode locking based on nonlinear polarization rotation [21, 22]. Unlike application of mode lockers [24, 25], the pulse width in our experiments without generic mode locking mechanisms (Fig. 2) was estimated to be of 40 ns. This means the approximation where the second order dispersion can be neglected is the context of the qualitative description of the experimentally observed vector resonance mode locking. The pulse width is also much longer than the time of transverse relaxation of 160 fs. For this reason, the dynamics of the medium polarization was also ignored [13-18].

To specify conditions for the vector resonance mode locking, we linearize the Eqs. (2) in the vicinity of the steady state solution $\boldsymbol{F}_0=(S_{00}\ \pm S_{00}\ 0\ 0\ f_{10}\ f_{20}\ 0)^T$ and find eigenvalues as follows (details are found in Supplementary Material [23]).

$$
\begin{aligned}
&(I)\quad \lambda_0 = iq + A_0(I_p,\xi),\\
&(II)\quad \lambda_1 = A_1(q,I_p,\xi) + i\Omega_1(q,I_p,\xi),\\
&\lambda_2 = A_2(q,I_p,\xi) + i\Omega_2(q,I_p,\xi),\\
&\lambda_3 = A_3(q,I_p,\xi) + i\Omega_3(q,I_p,\xi),\\
&(III)\quad \lambda_4 = A_4(q,I_p,\beta,\xi) + i\Omega_4(q,I_p,\beta,\zeta),\\
&\lambda_5 = A_5(q,I_p,\beta,\xi) + i\left(q + \Delta\Omega(q,I_p,\beta,\xi)\right),\\
&\lambda_6 = A_6(q,I_p,\beta,\xi) + i\left(q - \Delta\Omega(q,I_p,\beta,\xi)\right),\\
&A_0(I_p,\xi) > 0,\ A_1(q,I_p,\xi) < 0,\ \ A_2(q,I_p,\xi) < 0,\\
&A_3(q,I_p,\xi) < 0,\\
&A_4(q,I_p,\xi) < 0,\ A_5(q,I_p,\xi) > 0,\ A_6(q,I_p,\xi) > 0.
\end{aligned}
\tag{4}
$$

Here $q=0,\pm1,\pm2,..\pm N$ is the wave number of the longitudinal mode. All eigenvalues are normalized to the fundamental frequency $\omega=2\pi/\tau_R$. The obtained results are shown in Fig.3. The first and the second (multimode instability) thresholds can be found in Fig. 3 (a). Unlike RNGH instability where threshold pump values are different for excitation of different number of longitudinal modes [16], the threshold for all longitudinal modes is the same as follows from Fig. 3(a). The additional difference is that the second threshold of the multimode instability coincides with the first lasing threshold for circuitry polarized pump and the second threshold slightly exceeds the first one with increased pump anisotropy parameter $\xi$. Threshold for multimode instability (branch I) coincides with the threshold of birefringence-dependent RF satellites excitation (branch III). As follows from Fig. 3(b), the scalar branch II provides additional birefringence-independent satellites with the frequency splitting of 0.01f (f is the fundamental frequency) with respect to the longitudinal mode frequency q. Though real part of the corresponding eigenvalues, i.e. $A_1$,$A_2$ and $A_3$, are less than zero, the satellites can be excited through parametric phase locking with the frequencies of the branch I. As follows from Fig. 3 (c), increased birefringence strength can result in the resonance conditions where satellites frequencies for the longitudinal mode q (branch III) matches the frequency of the longitudinal mode q+N (where N is integer) from the branch I.

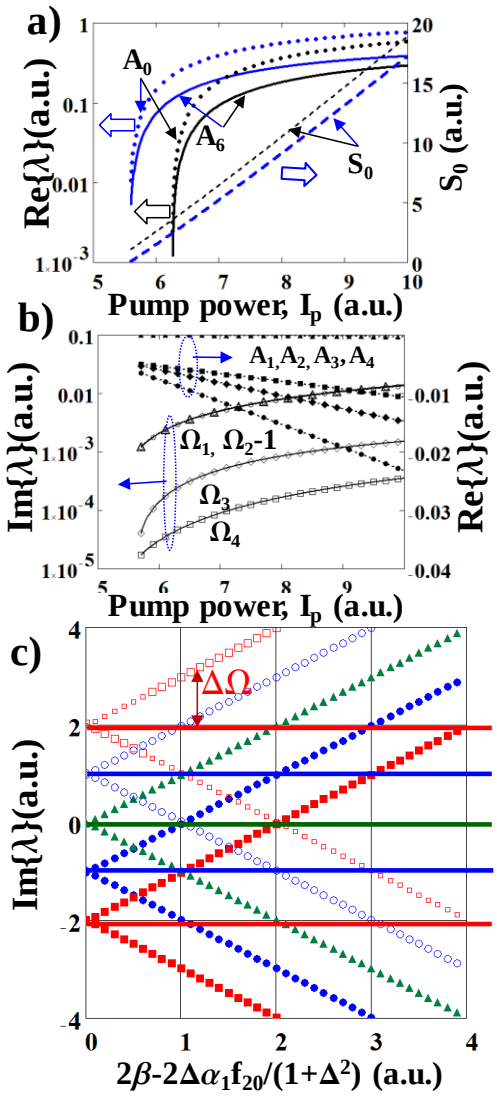


FIG. 3 (color online). The results of linear stability analysis of Eqs. (2). a) Vector multimode instability in terms of positive real parts of eigenvalues, i.e. $A_0$ (dots), $A_5$ (solid line) ($A_6$ is close to the $A_5$ and so is not shown here) and the output signal $S_0$ (dashed line) vs pump power $I_p$ for $\xi$=0 (blue lines), $\xi$=0.1 (black line); b) The frequencies of the scalar branch: $\Omega_1$ (empty circles) $\Omega_2$-1(empty triangles), $\Omega_3$ (empty squares) and vector branch $\Omega_4$ (empty diamonds) along with the real parts of the scalar branch: $A_1$ (filled circles), $A_2$ (filled triangles), $A_3$ (filled squares), and the vector branch: $A_4$ (filled diamonds) vs pump power $I_p$ for $\xi$=0.1. c) Frequencies for the branch I, i.e. $\Omega_0=\pm q$ , q=0,1,2,3 (solid lines), and the vector branch (III), i.e. $\Omega_{5,6}=q\pm\Delta\Omega$ (squares, triangles, circles), vs the birefringence strength $2\beta-2\Delta\alpha_1/(1+\Delta^2)$ for $\xi$=0.1. The equality $\Omega_0=\Omega_{5,6}$ for $2\beta-2\Delta\alpha_1/(1+\Delta^2)$=1,2,… means the resonance mode locking shown in Fig. 2(d2). Parameters: *L=615*

*m, $2\alpha_1$=ln(10)6.4, $2\alpha_2$=ln(10)0.5, $\chi_s$=3/2, $\chi_p$=1/0.7, $\Delta$=0.1, $I_p$=10 (c), $\gamma$=2x10$^{-6}$*, $\varepsilon=10^{-3}$, $\beta$=1 (a,b), q=1 (b), $\xi$=0.1 (b,c).

Thus, the theoretical results shown in Fig.3 are in a good correspondence with the experimental results shown in Figs.1 and 2. In both experiment and theory cases, the threshold of the multimode instability (the second threshold) slightly exceeds the first lasing threshold (Fig. 3 (a)). If the birefringence-dependence satellites frequencies deviates from the longitudinal mode frequencies (Fig.2 (a1-c1)) the complex oscillatory behavior emerges in view of equal threshold condition for all longitudinal modes (Fig. 3 (a)). The matching the longitudinal modes' frequencies with the birefringence-dependent satellites results in their synchronization similar to the mode locking scenario through the injection locking [20]. As follows from Figs. 2(b, c), matching the frequencies leading to the stable mode locking is accompanied with the stable SOP locking. The complexity of Eqs. (2) exceeds the complexity of any known scalar or vector models of fiber lasers considered for example in [16] and [26]. As follows from Fig. 3 even linear stability analysis results in the number eigenfrequencies with the ratio (with respect to the fundamental frequency) of $1:10^{-1}:10^{-2}:10^{-3}:10^{-4}$ . In addition to this, the presence of harmonics (more than 1000, as follows from the experiment) requires accounting for many time scales. In view of such complexity, the direct numerical simulation is beyond of the scope of our manuscript and so will be presented in our forthcoming publications.

In conclusion, we demonstrate experimentally and theoretically a new vector resonance multimode instability by using testbed erbium doped fiber laser. By adjusting the in-cavity and the pump wave polarization controllers we were able to tune the laser dynamics from the complex oscillatory to the periodic similar to the mode locked regime. The increased birefringence strength leads to generation of satellite lines from the q-harmonic frequency that in the case of resonance with the q+N –harmonic, i.e. case when N-fold beat length equals to the cavity length, results in longitudinal modes synchronization. This synchronization result in the pulse width deceasing to the value of 40 ns that much less than the round trip time of 3 $\mu$s. The demonstrated vector resonance multimode instability is a generic in the context of the spatial modulation of distributed system which leads to the spectral splitting. The resonance of the split satellites with the other branch of eigen-frequencies can lead to the synchronization phenomena which can be of interest in photonics and beyond. For example, the in-cavity birefringence depends on the ambient temperature and the mechanical stress in the fiber, and so the recognition and control of laser

regimes depending on environmental conditions is a challenging problem. In this context, the demonstrated approach of the stable vector resonance mapping can find potential applications for fiber laser stabilization based on machine learning using self-adjustment of the optimal laser parameters, i.e. power, the ellipticity of the pump wave and in-cavity birefringence [29]. In addition, vector resonance multimode instability demonstrated in this Letter can drive the emergence of spatially localized structures in the other laser systems, for example in vertical cavity surface emitting lasers [30].

We acknowledge support from the Leverhulme Trust (Grant ref: RPG-2014-304), FP7-PEOPLE-2012-IAPP (project GRIFFON, No. 324391).

REFERENCES

1. M. Tlidi et al. Theme Issue "Localized structures in dissipative media: from optics to plant ecology", *Phil. Trans. R. Soc. A* **372**, 20140006 (2014).
2. G. P. Agrawal, *Nonlinear fiber optics* (Academic press, San Diego, 2013).
3. V.E. Zakharov and L.A. Ostrovsky, *Physica D* **238**, 540 (2009).
4. T. B. Benjamin and J. E. Feir, *J. Fluid Mech.* **27**, 417 (1967).
5. M. Faraday, *Phil. Trans. R. Soc. London* **121**, 299 (1831).
6. Ch. Szwaj, S. Bielawski, D. Derozier, T. Erneux, *Phys. Rev. Lett.* **80**, 3968 (1998).
7. E. G. Turitsyna et al., *Nature Photon.* **7**, 783 (2013).
8. M. Onorato et a. *Phys. Rev. Lett.* **102,** 114502 (2009).
9. A. M. Perego, N. Tarasov, D. V. Churkin, S. K. Turitsyn, and K. Staliunas, *Phys. Rev. Lett.* **116**, 028701 (2016).
10. H. Risken and Nummedal, *Phys. Lett. A* **26**, 275 (1968).
11. H. Risken and Nummedal, *J. Appl. Phys.* **39**, 4662 (1968)
12. R. Graham and H. Haken, *Z. Phys.* **213**, 420 (1968).
13. F. Fontana, M. Begotti, E. M. Pessina, and L. A. Lugiato, *Opt. Commun.* **114**, 89 (1995).
14. E. M. Pessina, G. Bonfrate, F. Fontana, and L. A. Lugiato, *Phys. Rev. A* **56**, 4086 (1997).
15. E. M. Pessina, F. Prati, J. Redondo, E. Roldán, and G. J. de Valcárcel, *Phys. Rev. A* **60**, 2517 (1999).
16. E. Roldán, G. J. de Valcárcel, F. Prati, F. Mitschke, and T. Voigt, 2004. arXiv preprint physics/0412071 (2004).

17. T. Voigt, M. Lenz, F. Mitschke, E. Roldán, and G. J. de Valcárcel, *Appl. Phys. B* **79**, 175 (2004).
18. L. Lugiato, F. Prati, M. Brambila. Nonlinear Optical Systems (Cambridge University Press, Cambridge, 2015).
19. S. A. Kolpakov, H. Kbashi, and S V. Sergeyev, *Optica*, **3** , 870 (2016).
20. S. T. Cundiff, J. and Ye, *Rev. Mod. Phys.* **75**, 325 (2003).
21. C. Lecaplain, Ph. Grelu, S. Wabnitz, *Phys. Rev. A* **89**. 063812-1-10 (2014).
22. H. Lee, G. P. Agrawal, *IEEE J. Quant. Electron.* **46**, 1732-1738 (2010).
23. See Supplementary Material at … for more details on the stability analysis.
24. S.V. Sergeyev et al. *Light: Science & Applications* **3**, e131 (2014).
25. S. V. Sergeyev. *Phil. Trans. R. Soc. A* **372**, 20140006 (2014).
26. H. Zeghlache, A. Boulnois. *Phys. Rev. A* **52**, 4229 (1995).
27. R. Leners, G. Stéphan G. *Quantum. Semiclass. Opt.* **7,** 757 (1995).
28. S. V. Sergeyev. *Phys. Rev. A* **59**, 3909- 3917 (1999).
29. X. Fu, S. L. Brunton, and J. N. Kutz, *Opt. Express* **22**, 8585 (2014).
30. E. Averlant, M. Tlidi, H. Thienpont, T. Ackemann, and K. Panajotov, Sci. Reports, **6** (2016)